Proceedings of Global Power and Propulsion Society
ISSN-Nr: 2504-4400
GPPS Hong Kong 2023
October 17-19, 2023
www.gpps.global

GPPS-TC-2023-0263

EXPERIMENTAL INVESTIGATION ON THE EFFECT OF IMPINGEMENT HOLE LOCATION ON VANE IMPINGEMENT/FILM COOLING

Xiang Cheng
Key Laboratory of Thermo-Fluid Science and Engineering of MOE, Xi'an Jiaotong University
chengxiang2019@foxmail.com
Xi'an, Shaanxi, China

Yu-Zhong Ding
Key Laboratory of Thermo-Fluid Science and Engineering of MOE, Xi'an Jiaotong University
Dingyuzhong@stu.xjtu.edu.cn
Xi'an, Shaanxi, China

Hong-Niu Wan
Key Laboratory of Thermo-Fluid Science and Engineering of MOE, Xi'an Jiaotong University
3499528354@qq.com
Xi'an, Shaanxi, China

Wen-Tao Ji
Key Laboratory of Thermo-Fluid Science and Engineering of MOE, Xi'an Jiaotong University
wentaoji@xjtu.edu.cn
Xi'an, Shaanxi, China

Ya-Ling He
Key Laboratory of Thermo-Fluid Science and Engineering of MOE, Xi'an Jiaotong University
yalinghe@mail.xjtu.edu.cn
Xi'an, Shaanxi, China

Wen-Quan Tao
Key Laboratory of Thermo-Fluid Science and Engineering of MOE, Xi'an Jiaotong University
wqtao@mail.xjtu.edu.cn
Xi'an, Shaanxi, China

ABSTRACT

In order to study the effect of impingement hole location on the ICE (Integrated Cooling Effectiveness) of turbine vanes, the heat transfer experiments of vanes with low thermal conductivity were conducted. The test vanes include typical film cooling without jets (Vane 0), typical impingement/film cooling with centerline normal jets (Vane 1), and swirl impingement/film cooling with offset jets (Vane 2). When the *BR* (Blowing Ratio) was relatively higher, the heat transfer between the coolant and the target surface was enhanced by jet impingement, and the ICE of Vanes 1 and 2 was 3.6-8.6% higher than that of Vane 0. The jet impingement enhanced region was relatively independent of the film hole coverage region because the offset impingement holes were located at the film hole inlet upstream. It made the vane surface temperature distribution more uniform and ICE of Vane 2 slightly higher. However, when the *BR* was relatively small, the ICE of Vane 1 with centerline jets was larger than that of Vane 0, and the ICE of Vane 2 with offset jets was lower than that of Vane 0.

INTRODUCTION

With the development of aeroengine technology, the turbine first stage mainstream temperature has exceeded the limiting temperature of turbine vane material (Bohn et al., 1999, Bunker, 2005, Boyce, 2011, Nourin and Amano, 2021, Zhang et al., 2023). To improve the safety and stability of aviation engines, it is crucial to develop efficient cooling technology (Nourin and Amano, 2021, Unnikrishnan and Yang, 2022). Turbine vane cooling technology mainly includes internal cooling technology and external cooling technology. For turbine vane leading cavity, impingement/film combined cooling are usually adopted (Nourin and Amano, 2021, Zhang et al., 2022a, Cheng et al., 2023).

In order to further optimize the cooling structure design and reasonably distribute the cooling gas, a lot of studies have been conducted on different cooling technologies. Rao et al. (Rao et al., 2016) investigated the influence of W-shaped ribs on impingement cooling characteristics of flat plates. Experimental and numercial results indicate that micro-W-rib can increase the impingement cooling effectiveness by 9.6% or more. Lyu et al. (Lyu et al., 2019) carried out experiments to study the influence of the impingement target surface curvature, nozzle geometry, the length between the nozzle and the target plates, and Reynolds number on the impingement cooling effectiveness. Experimental data indicate that the cooling effect is best at the concave surface leading edge, and the chevron nozzle has the better cooling effect when the impingement distance is smaller. Deng et al. (Deng et al., 2022) experimentally investigated the cooling characteristics of impingement

cooling under rotating conditions. Experimental results show that when rotation number does not reach the critical value, the influence of buoyancy can be ignored. Li et al. (Li et al., 2022) experimentally studied the influence of channel orientation on cooling characteristics. The experimental results show that obvious heat transfer deterioration occurred in the large channel orientation and large rotation number region. In addition to studying impingement cooling separately, many studies have focused on the cooling characteristics of impingement/film combined cooling. Chen et al. (Chen et al., 2019) numerically investigated the conjugate cooling characteristics of impingement/film cooling under different crossflow schemes. Relevant results show that the performance of composite cooling is superior to that of a single cooling method. The blocked maximum crossflow case proposed in this paper has optimal cooling effect. Fawzy et al. (Fawzy et al., 2020) numerically investigated the influence of different distribution positions of nozzles (tangent, inline normal, staggered normal) on the impingement/film cooling conjugate heat transfer. Numerical results indicate that the overall Nusselt number of the staggered normal scheme has increased by a maximum of 21.27% compared to the other two schemes. Kwon et al. (Kwon et al., 2022) used the flat plate model to numerically investigate the conjugate cooling characteristics of impingement/film combined cooling. The results reveal the flow field distribution and local cooling characteristics on both sides of the target surface (hot side and cold side). Singh and Udayraj (Singh and Udayraj, 2022) numerically studied the influence of film hole forward and reverse arrangements on impingement/film cooling. Relevant research results indicate that the cooling effect for forward film hole is better when the blowing ratio is small. However, when the *BR* is relatively high, reverse film hole damage kidney-vortices, thereby enhancing the cooling effect. However, these studies were conducted in simplified models, which is significantly different from the real cooling structure of engines. To obtain the cooling mechanism of actual turbine vanes, it is essential to conduct conjugate heat transfer experiments on actual turbine vane profiles. Although some studies (Yang et al., 2019, Liu et al., 2020, Zhang et al., 2022a) have also been carried out in actual blade profiles, few relevant research has been conducted on turbine stator vane impingement/film cooling.

In order to apply impingement/film cooling to the turbine vane leading cavity, integrated cooling effectiveness experiments were conducted. The experimental vane profile is derived from an actual turbine vane. The effects of the blowing ratio and the relative position of the film hole and the impingement hole on the cooling performance were investigated. Despite the fact that this Biot number is not matched with real engine, the relevant experimental results can still provide reference for the design of turbine vane cooling structures and can be used to verify the accuracy of numerical simulation results.

METHODOLOGY

Experimentla system

As shown in Figure 1, the vane integrated cooling effectiveness experiments were conducted on turbine vane cooling characteristics testing experimental system. The maximum volume flow of mainstream is 87.6 Nm^3/min, the maximum volume flow of secondary flow is 7.65 Nm^3/min, and the maximum temperature of mainstream can reach 500 K.

The mainstream gas is supplied by two compressors. The gas from the compressors flows through the refrigeration dryers and filters in sequence, then enters the storage container. The mainstream gas quantity entering the linear cascade is jointly controlled by a vortex flowmeter (±1%) and bypass valve.

The secondary flow gas (coolant) is supplied by a compressor. Like mainstream gas, secondary flow gas also flows through the refrigeration dryer, filter, and then enters the air tank. The coolant temperature is controlled by a secondary flow heater, and the gas quantity entering the linear cascade is controlled by mass flow controllers (±1%). In order to ensure independent gas supply to the two cooling cavities of the vane, there are two branches for the secondary flow. In this study, only one branch was used.

The geometric shape of linear cascade is determined by parameters such as real turbine vane mid-section profile, vane height, vane spacing, and so on. The linear cascade consists of a test vane and two complete gas flow channels. The wall on the vane pressure surface side is processed into the configuration of the vane suction surface, the wall on the suction surface side is processed into the configuration of the vane pressure surface and the rotatable trailing edge plate is arranged at the cascade outlet. Through all the above measures ensure the experiment periodicity. Five-hole probe, turbulence grid, temperature probe (±0.1%), and hot wire probe are installed at different positions of linear cascade inlet. Among them, the five-hole probe is used to meter the inlet total pressure, static pressure and inlet velocity. The temperature probe is used to meter the mainstream gas inlet temperature. The hot wire probe is used to measure the inlet turbulence intensity. This turbulence intensity measured in this study was 11%. The infrared window is installed on the test vane pressure surface side. The temperature distribution on the outer surface of the test vane was measured by an infrared camera (FLIR T630sc, ±2%).

In order to reduce experimental noise, a silencer is installed at the experimental system outlet. The gas after the experiment was discharged into the atmospheric environment after passing through the muffler and condensation tower.

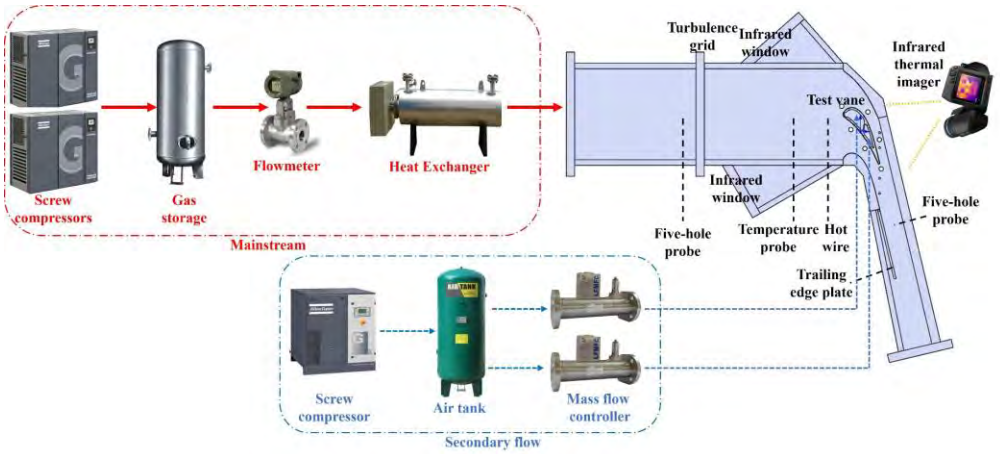

Figure 1 Experimental System

Test vane

There are three test vanes in this study. The test vanes' cooling structures distribution is shown in Figure 2. All test vanes were processed using 3D printing, and the vane material is a low thermal conductivity photosensitive resin. Among them, Vane 0 is the basic vane with only film cooling structures, Vane 1 and Vane 2 are with impingement/film cooling structures. The vane geometric parameters and cooling structures arrangement are derived from the actual turbine vane. Two cylindrical film hole rows are arranged on the pressure surface, with the angle of 30° between extension direction of the film hole centerline and the vane profile tangent, and 90° between extension direction of the film hole centerline and the vane height direction. For Vane 1 and Vane 2, each film hole row corresponds to an independent impingement cavity. The impingement cavity is connected to the cooling cavity through the impingement holes. For Vane 1, coolant jet impingement along the impingement cavity centerline, while for Vane 2, the coolant jet impingement position is offset upstream of the film hole inlet. The diameter (D) of film hole is 1.0 mm, and the diameter (D_i) of impingement hole is 2.0 mm. The film hole number in Row 1 is 35, and that in Row 2 is 34. The number of impingement holes in both rows is 10.

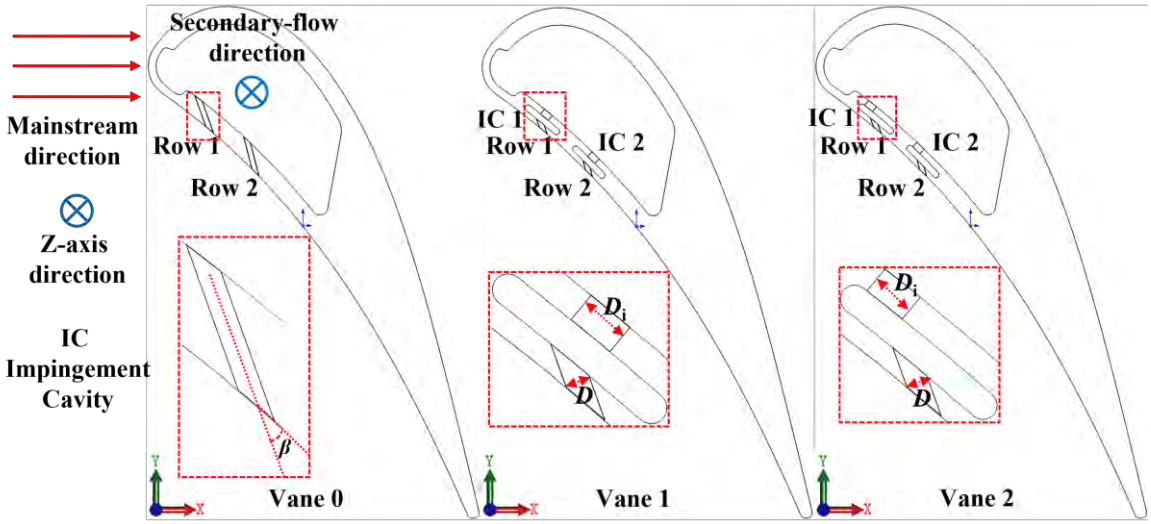

Figure 2 Test Vane Cooling Structures Distribution

Experimental conditions

The blowing ratio (BR) is calculated using the following formula.

$$BR = \frac{\rho_c U_c}{\rho_g U_g} \qquad (1)$$

where, ρ_c and ρ_g represent the secondary flow density and mainstream density, respectively. U_c and U_g represent the secondary flow velocity and mainstream velocity, respectively. Because the mainstream velocity used to calculate the BR is the cascade inlet velocity, but not the local velocity. So the BR in this study is a global value not a local one.

The Reynolds number (Re_{in}) of linear cascade inlet is defined as follows.

$$Re_{in} = \frac{\rho_g U_g C}{\mu_g} \qquad (2)$$

where, C represents the test vane chord length, μ_g represents the mainstream dynamic viscosity.

Integrated cooling effectiveness (φ, ICE) is calculated using the following formula.

$$\varphi = \frac{T_g - T_w}{T_g - T_c} \qquad (3)$$

where, T_g, T_c, and T_w represent the mainstream, secondary flow and test vane outer wall surface temperatures, respectively.

The relative uncertainty of the linear cascade inlet Reynolds number ($u_{rel}(Re_{in})$) and ICE ($u_{rel}(\varphi)$) is shown below (Coleman and Steele, 1995).

$$u_{rel}\left(Re_{in}\right) = \sqrt{\frac{u^2\left(\rho_g\right)}{\left(\rho_g\right)^2} + \frac{u^2\left(U_g\right)}{\left(U_g\right)^2} + \frac{u^2\left(\mu_g\right)}{\left(\mu_g\right)^2}} \qquad (4)$$

$$u_{rel}\left(\varphi\right) = \sqrt{\frac{u^2\left(T_g\right)+u^2\left(T_w\right)}{\left(T_g - T_w\right)^2} + \frac{u^2\left(T_g\right)+u^2\left(T_c\right)}{\left(T_g - T_c\right)^2}} \qquad (5)$$

where, $u(\rho_g)$, $u(U_g)$, $u(\mu_g)$, $u(T_g)$, $u(T_c)$, and $u(T_w)$ mean the standard uncertainty of density, velocity, dynamic viscosity, temperature of mainstream gas, temperature of secondary-flow gas, and temperature of test vane outer surface, respectively. The relative uncertainty of the Reynolds number and ICE is 2.14% and 4.03%, respectively.

The experimental conditions of this study are shown in Table 1. In this table, p_g represents the linear cascade inlet static pressure.

Table 1 Experimental conditions

No	Vane	p_g/ kPa	T_g/ K	U_g/ m/s	Re_{in}	T_c/ K	BR
1	Vane 0	47	323.5	27.1	2.3×10^5	297.5	0.2-2.0
2	Vane 1	47	323.5	27.1	2.3×10^5	297.5	0.2-2.0
3	Vane 2	47	323.5	27.1	2.3×10^5	297.5	0.2-2.0

RESULTS AND DISCUSSION

Temperature measurement calibration

According to the methods in references (Zhang et al., 2022b) and (Cheng et al., 2023), the infrared thermal imager was calibrated. During the calibration process, high-precision thermocouples and infrared thermal imagers are used to simultaneously monitor the temperature at the same measuring point. Measuring plate is heated by the heating film. Change the heating power to obtain calibration data at different temperatures. Spray matte black paint consistent with that used for test vanes on the measuring plate. The temperature measurement calibration data is shown in Figure 3. Subsequently, the temperature data of the infrared thermal imager is processed based on the fitted curve in the figure.

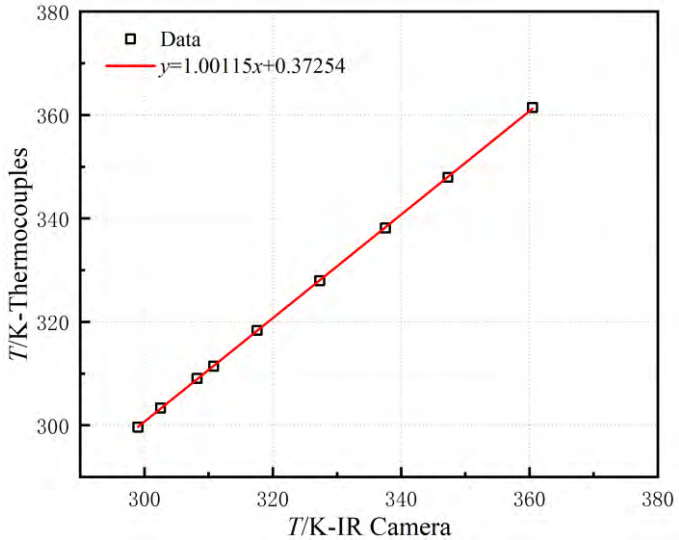

Figure 3 Temperature measurement calibration

Effect of Blowing Ratio

Figure 4 shows the distribution of ICE at different BRs. The corresponding experimental condition is Case No. 3, and the test vane is Vane 2. The horizontal coordinates s/C and the vertical coordinates z/H represent the dimensionless position on the vane outer surface. Among them, s means the distance from the local measurement point to the leading edge, z

means the distance from the local measurement point to the vane root, C means the vane chord length, and H means the vane height.

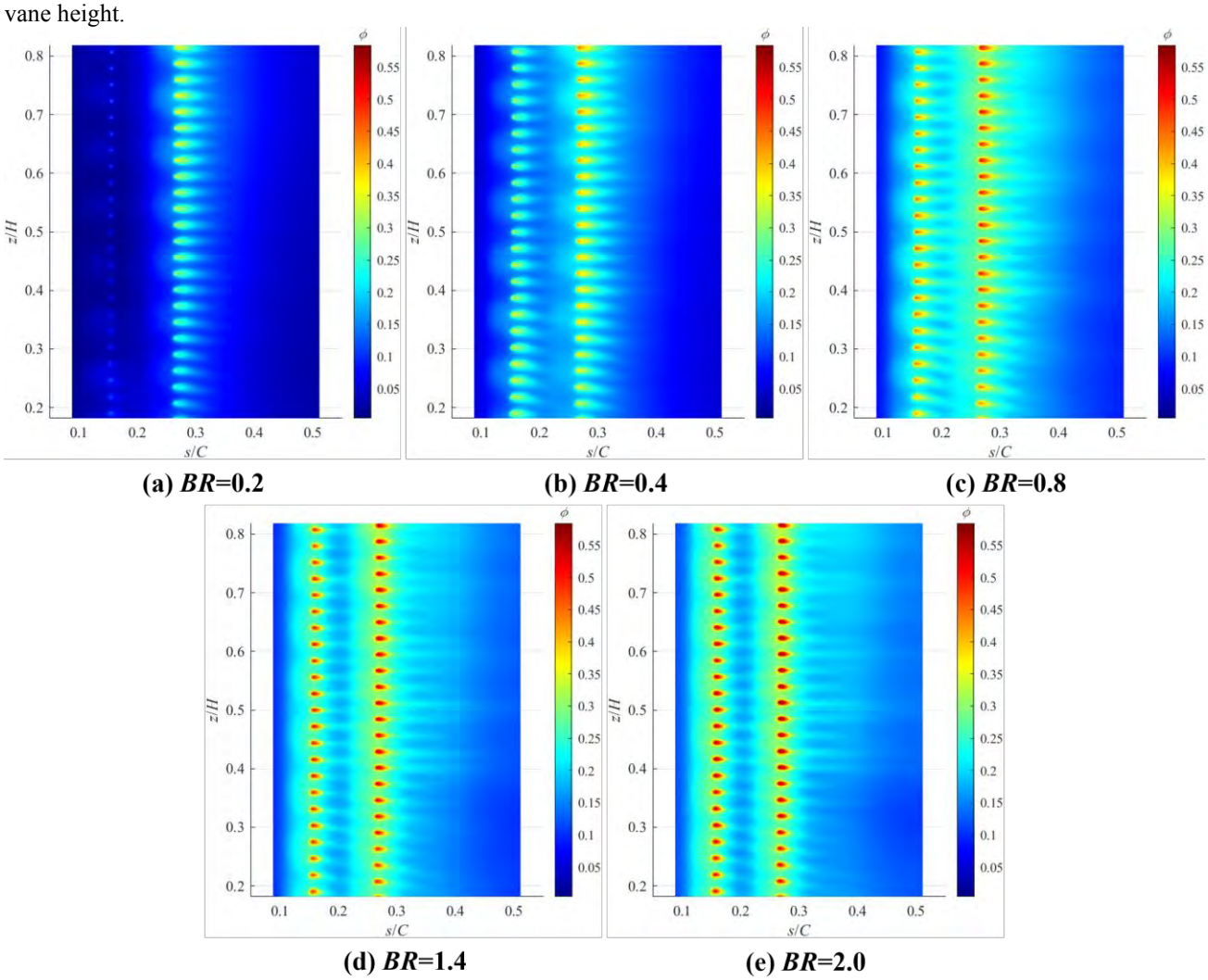

Figure 4 ICE Distribution Under Different *BR*s (Case No. 3)

As shown in Figure 4, as the *BR* increased, ICE gradually increased. When *BR* was small (*BR*=0.2, 0.4), the coolant volume was insufficient, making it difficult to form effective thermal protection on the vane surface. As *BR* increased, the coolant volume increased, forming the wide coverage film on the vane surface. At the same time, the cooling effect of jet impingement was also enhanced, and the ICE increased. When *BR* was equal to 0.2 and 0.4, it could be clearly observed that the cooling effect in Row 1 region was significantly weaker than that in Row 2 region. This was caused by different static pressure. The surface static pressure of the vane pressure surface gradually decreased from the leading edge to the trailing edge (Cheng et al., 2023, Zhang et al., 2023). The surface static pressure of Row 1 region was higher than that of Row 2 region. Therefore, the obstruction of the coolant outflow in Row 2 region was smaller than that in Row 1 region and the cooling effect in Row 1 region was significantly weaker than that in Row 2 region. In addition, local ICE fluctuations could also be observed in the vane spanwise (coolant flow direction). This was because the larger region of ICE corresponded to the impingement hole jet impingement region. Due to impingement cooling, the temperature in this region decreased and the cooling effect was enhanced.

Figure 5 shows the spanwise- and overall-averaged ICE (φ_{ave}, φ_{ove}) distribution under different *BR*s. As shown in Figure 5(a), the ICE of Row 1 region was smaller than that of Row 2 region, and the smaller the *BR*, the more significant this difference. With the increase of *BR*, ICE continued to increase, but the growth rate of ICE growth changed. When the *BR* increased from 0.2 to 0.8, the overall-averaged ICE increased by 163.4%, and for *BR* increased from 0.8 to 2.0, that only increased 13.9%. This was because when *BR* increased from 0.2 to 0.8, the cooling effectiveness of impingement cooling and film cooling simultaneously increased, resulting in a higher growth rate of ICE. During the process of *BR* increasing from 0.8 to 2.0, the coolant detached from the wall after flowing out of the film hole, resulting in the decrease of film cooling effectiveness. However, the cooling effectiveness of impingement cooling still increased, so the growth rate of ICE decreased.

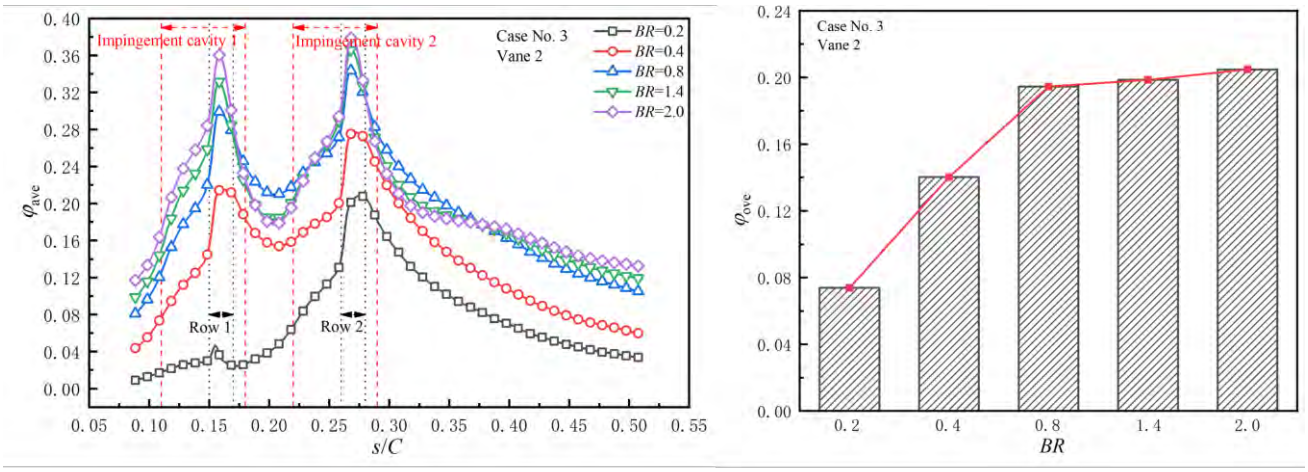

(a) Spanwise-averaged ICE (b) Overall-averaged ICE

Figure 5 Spanwise- And Overall-averaged ICE Under Different *BR*s (Case No. 3)

Effect of impingement hole location

Figure 6 shows the distribution of ICE for different test vanes under different *BR* conditions. Among them, Figure 6(a)(b)(c) corresponds to *BR*=0.2, and Figure 6(d)(e)(f) corresponds to *BR*=0.8.

As shown in Figure 6, the ICE distribution varied greatly among different test vanes under the same *BR*. When *BR*=0.2, the overall cooling effect was poor because the small coolant flow rate. In Row 1 region, the ICE was lower and the gas film coverage was smaller. In Row 2 region, along the coolant flow direction, ICE gradually decreased. This was because the heat exchange between the coolant and the test vane leading cavity inner wall, as well as the suction effect of the film hole, the downstream coolant temperature increased and the gas volume decreased, resulting in the decrease of ICE. As shown in Figure 6(b)(c), unlike Figure 6(a) Vane 0, there was significant local peaks of ICE at the impingement target surface corresponding to the impingement holes in the Row 2 region. However, as the impingement holes of Vane 2 was located upstream of the film hole inlet, the local peaks of Vane 2 also appeared upstream. When *BR*=0.8, the vane cooling effectiveness had been greatly improved. However, compared to Vane 0 in Figure 6(d), the ICE distribution of Figure 6(e) Vane 1 and Figure 6(f) Vane 2 was more uniform, especially in the upstream and downstream regions of the film hole outlet, where ICE increased significantly. This was because impingement/film cooling further improved the coolant utilization rate, and further reduced the vane surface temperature within the impingement cavity coverage range. As shown in Figure 6(e)(f), the ICE of Vane 2 improved compared to Vane 1, especially in the Row 2 region, with the significant improvement. In the Row 2 region, upstream of the Vane 2 film hole outlet, the efficient cooling region of the impingement target surface expanded, and the ICE was relatively high and evenly distributed along the coolant flow direction.

Figure 7 shows the spanwise-averaged ICE (φ_{ave}) distribution for different test vanes under different *BR* conditions. As shown in Figure 7(a), in the Impingement Cativity 1 region, Vane 0 had the highest spanwise-averaged ICE. This was because at *BR*=0.2, the coolant flow rate was small and the kinetic energy was also small. Additionally, due to the absence of the impingement cooling in Vane 0, corresponding flow resistance of the coolant flowing out was small. Therefore, in the Impingement Cativity 1 region, Vane 0 had the highest spanwise-averaged ICE. In the Impingement Cavity 2 region, as the coolant flow rate increased relative to Impingement Cavity 1 region, impingement cooling began to dominate. However, due to the impingement holes of Vane 2 being located upstream of the film hole inlet, corresponding resistance of the secondary flow flowing out of the leading cavity was greater than Vane 1, so Vane 1 had the highest ICE in this region. At *BR*=0.2, the overall-averaged ICE of Vane 1 increased by 8.6% compared to Vane 0, while Vane 2 decreased by 6.7%. As shown in Figure 7(b), *BR* increased to 0.8, and the spanwise-averaged ICE of Vane 2 was the highest in the vast range of *s/C*=0.1-0.3. This was because as *BR* increased, the kinetic energy of the coolant increased. Meanwhile, the jet impingement target of Vane 2 did not coincide with the downstream of the film hole outlet, and the cooling capacity of the coolant was maximized. However, after *s/C*>0.32, the spanwise-averaged ICE of Vane 0 was the highest. This was because at *BR*=0.8, for Vane 0, the coolant flowed out of the film hole first detached from the vane outer surface and then reattached to the wall as the coolant and mainstream continue to mix. Therefore, after *s/C*>0.32, the coolant of Vane 0 reattached to form the gas film, while the coolant of Vane 1 and Vane 2 did not reattache, but gradually dissipated. Therefore, within this range, Vane 0 had the highest ICE. At *BR*=0.8, the overall-averaged ICE of Vane 1 and Vane 2 increased by 3.6% and 5.3% compared to Vane 0, respectively.

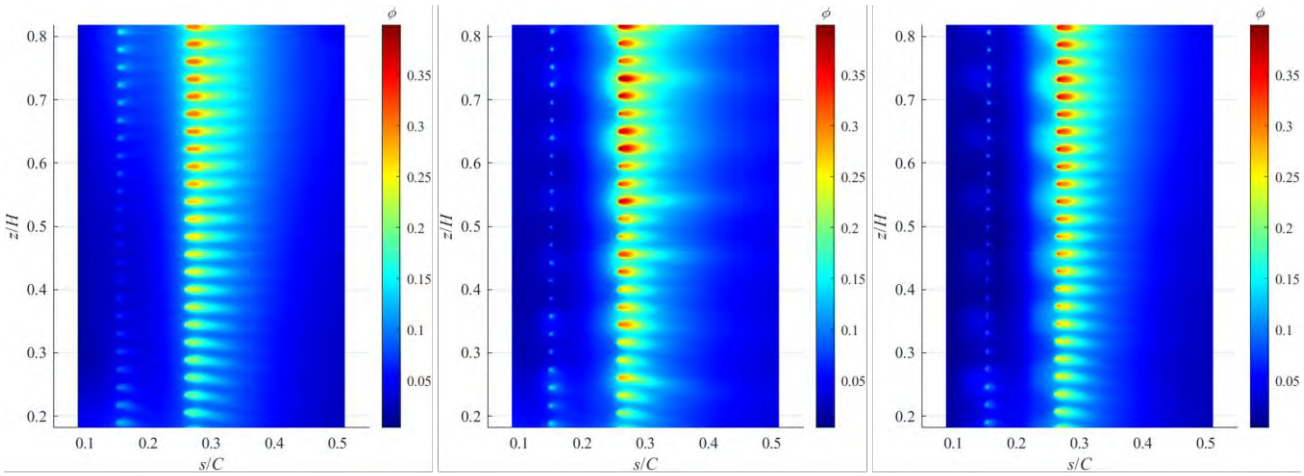

(a) Vane 0, *BR*=0.2 (b) Vane 1, *BR*=0.2 (c) Vane 2, *BR*=0.2

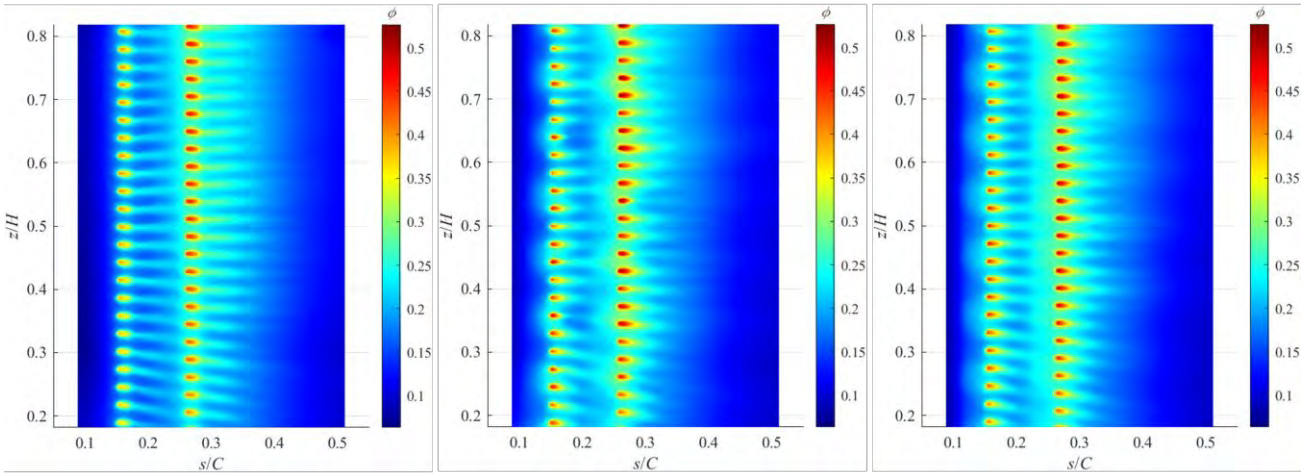

(d) Vane 0, *BR*=0.8 (e) Vane 1, *BR*=0.8 (f) Vane 2, *BR*=0.8

Figure 6 ICE Distribution For Different Test Vanes

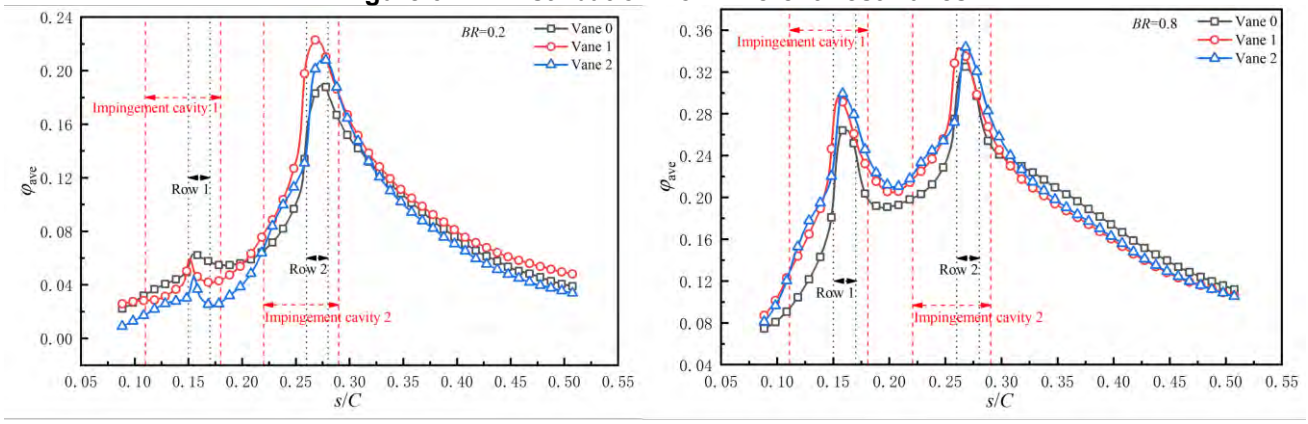

(a) *BR*=0.2 (b) *BR*=0.8

Figure 7 Spanwise-averaged ICE For Different Test Vanes

CONCLUSIONS

In order to optimize the cooling structure design and coolant flow distribution of the turbine stator vanes leading cavity, this paper conducted flow and heat transfer experiments on low thermal conductivity turbine vanes. The experiment included three test vanes, namely Vane 0 (typical film cooling without jets), Vane 1 (typical impingement/film cooling with centerline normal jets), and Vane 2 (swirl impingement/film cooling with offset jets). The experiments explored the effect of *BR* (Blowing Ratio) and the impingement hole location on integrated cooling effectiveness.

The main conclusions obtained are presented below.

(1) The ICE of the vane outer surface was determined by both internal and external cooling. For the test vanes in this study, as *BR* increased, ICE also increased. However, due to the different changes in external film cooling effectiveness and internal forced convection cooling and impingement cooling effectiveness with *BR* increease, ICE growth rate gradually decreased.

(2) Due to the difference in static pressure on the vane outer surface, the ICE in Row 1 region was smaller than that in Row 2 region. And this trend became more pronounced as *BR* decreased.

(3) When the *BR* was smaller (*BR*=0.2), due to the different position of the impingement holes and the offset jet impingement consumed more coolant kinetic energy. Therefore, the ICE of Vane 1 and Vane 2 increased by 8.6% and decreased by 6.7% compared to Vane 0, respectively.

(4) When the *BR* was larger (*BR*=0.8), the impingement target region by the offset jet did not coincide with the film cooling coverage region. Therefore, the overall-averaged ICE of Vane 1 and Vane 2 increased by 3.6% and 5.3% compared to Vane 0, respectively.

NOMENCLATURE

φ_{ove}	Overall-averaged integrated cooling effectiveness
s	Arc length, mm
ρ_g	Mainstream density, kg · m^{-3}
β	Hole skew angle, °
D	Film hole diameter, mm
ICE	Integrated Cooling Effectiveness
ρ_c	Coolant density, kg · m^{-3}
α	Hole slant angle, °
U_c	Coolant velocity, m · s^{-1}
Re_{in}	linear cascade inlet Reynolds number
z	Local vane height, mm
U_g	Mainstream velocity, m · s^{-1}
C	Vane chord length, mm
T_c	Coolant temperature, K
T_w	Wall temperature, K
μ_g	Mainstream dynamic viscosity, Pa · s
T_g	Mainstream temperature, K
H	Vane height, mm
p_g	Mainstream inlet static pressure, Pa
φ	Integrated cooling effectiveness
D_i	Impingement hole diameter, mm
BR	Blowing Ratio
φ_{ave}	Spanwise-averaged integrated cooling effectiveness

ACKNOWLEDGMENTS

This work was supported by the National Science and Technology Major Project (2017-III-0003-0027).

References

BOHN, D. E., BECKER, V. J., KUSTERER, K. A., OTSUKI, Y., SUGIMOTO, T. & TANAKA, R. 1999. 3-D Internal Flow and Conjugate Calculations of a Convective Cooled Turbine Blade With Serpentine-Shaped and Ribbed Channels. *Volume 3: Heat Transfer; Electric Power; Industrial and Cogeneration.*

BOYCE, M. P. 2011. *Gas Turbine Engineering Handbook,* Waltham, Butterworth-Heinemann.

BUNKER, R. S. 2005. A Review of Shaped Hole Turbine Film-Cooling Technology. *Journal of Heat Transfer,* 127**,** 441-453.

CHEN, G., LIU, Y., RAO, Y., HE, J. & QU, Y. 2019. Numerical investigation on conjugate heat transfer of impingement/effusion double-wall cooling with different crossflow schemes. *Applied Thermal Engineering,* 155**,** 515-524.

CHENG, X., LI, Z.-R., WAN, H.-N., JI, W.-T., HE, Y.-L. & TAO, W.-Q. 2023. Effect of mass flow ratios on the conjugate heat transfer of a metal turbine vane at medium temperature. *International Journal of Heat and Mass Transfer,* 209**,** 124096.

COLEMAN, H. W. & STEELE, W. G. 1995. Engineering application of experimental uncertainty analysis. *AIAA Journal,* 33**,** 1888-1896.

DENG, H., LI, H. & XU, J. 2022. Heat transfer in an impingement cooling channel under isothermal boundaries at high rotation numbers. *International Journal of Heat and Mass Transfer,* 182**,** 121940.

FAWZY, H., ZHENG, Q., JIANG, Y., LIN, A. & AHMAD, N. 2020. Conjugate heat transfer of impingement cooling using conical nozzles with different schemes in a film-cooled blade leading-edge. *Applied Thermal Engineering,* 177**,** 115491.

KWON, H., LIGRANI, P. M., VANGA, S. R. & PARK, H. 2022. Flow structure and surface heat transfer from numerical predictions for a double wall effusion plate with impingement jet array cooling. *International Journal of Heat and Mass Transfer,* 183**,** 122049.

LI, H., DENG, H. & QIU, L. 2022. Effect of channel orientation on heat transfer in a rotating impingement cooling channel. *International Journal of Heat and Mass Transfer,* 187**,** 122493.

LIU, Z., LI, F., ZHANG, Z., FENG, Z. & SIMON, T. W. 2020. Conjugate Heat Transfer Predictions on Combined Impingement and Film Cooling of a Blade Leading Edge Model. *Heat Transfer Engineering,* 42**,** 1363-1380.

LYU, Y., ZHANG, J., LIU, X. & SHAN, Y. 2019. Experimental study of single-row chevron-jet impingement heat transfer on concave surfaces with different curvatures. *Chinese Journal of Aeronautics,* 32**,** 2275-2285.

NOURIN, F. N. & AMANO, R. S. 2021. Review of Gas Turbine Internal Cooling Improvement Technology. *Journal of Energy Resources Technology,* 143**,** 080801.

RAO, Y., CHEN, P. & WAN, C. 2016. Experimental and numerical investigation of impingement heat transfer on the surface with micro W-shaped ribs. *International Journal of Heat and Mass Transfer,* 93**,** 683-694.

SINGH, K. & UDAYRAJ 2022. Combined film and impingement cooling of flat plate with reverse cooling hole. *Applied Thermal Engineering,* 208**,** 118224.

UNNIKRISHNAN, U. & YANG, V. 2022. A review of cooling technologies for high temperature rotating components in gas turbine. *Propulsion and Power Research,* 11**,** 293-310.

YANG, X., LIU, Z., ZHAO, Q., LIU, Z., FENG, Z., GUO, F., DING, L. & SIMON, T. W. 2019. Experimental and numerical investigations of overall cooling effectiveness on a vane endwall with jet impingement and film cooling. *Applied Thermal Engineering,* 148**,** 1148-1163.

ZHANG, R., LUO, C., ZHOU, L., LI, L., ZHANG, H. & DU, X. 2022a. Impingement/film cooling of C3X vane with double-wall cooling structure using air/mist mixture. *International Journal of Heat and Mass Transfer,* 188**,** 122594.

ZHANG, W., LI, F., JIA, Z., LIU, Z., FENG, Z. & ZHANG, Y. 2022b. Experimental study on performance verification test of optimized film cooling holes in a linear cascade. *Applied Thermal Engineering,* 212.

ZHANG, W., LI, F., XIE, Y., DING, Y., LIU, Z. & FENG, Z. 2023. Experimental and numerical investigations of discrete film holes cooling performance on a blade endwall with mid-passage gap leakage. *International Journal of Heat and Mass Transfer,* 201**,** 123550.